

> REPLACE THIS LINE WITH YOUR MANUSCRIPT ID NUMBER (DOUBLE-CLICK HERE TO EDIT) <

A Radiometric Block Adjustment Method for Unmanned Aerial Vehicle Images Considering the Image Vignetting

Wanshan Peng, Yan Gong, Shenghui Fang, Yongjun Zhang, Jadunandan Dash, Jie Ren, Jiakai Mo

Abstract—Unmanned aerial vehicles (UAVs) equipped with different sensors can provide data with high spatiotemporal resolution and have broad application prospects. During the flight of the UAV, changes in illumination, exposure time, etc., will cause different degrees of radiometric differences between images, resulting in a calibration relationship established on a single image that cannot be applied to other images; in addition, the vignetting effect also significantly changes the brightness distribution inside an image, thus posing challenges for radiometric calibration of UAV images. In this paper, based on block adjustment (BA), we proposed a radiometric block adjustment model under the consideration of vignetting and the light-dark differences between images. The proposed method requires only a small number of calibration blankets, thus reducing the complexity of the experiment. The results from two study areas showed that the proposed method could compensate for vignetting to a certain extent and the radiometric consistency of the two datasets was improved from 13.16%~21.82% to 5.47%~12.72%. Validated using ground samples, the mean RMSE and MRPE of all five bands were 0.053, 21.6%, and 0.037, 20.4% in the two study areas, respectively. The total uncertainty was less than 7%. When there were obvious light-dark differences between images, such as in the visible light bands, our method could significantly improve the accuracy of the radiometric calibration.

Index Terms—block adjustment (BA), light-dark differences, radiometric calibration, unmanned aerial vehicles (UAVs), vignetting

I. INTRODUCTION

Unmanned aerial vehicles (UAVs) equipped with different sensors can provide data with high spatial and temporal resolution [1], thus offering great prospects for various applications, such as agriculture monitoring [2-4], plant phenotyping [5, 6], environmental monitoring [7, 8], meteorology [9], and archaeology [10, 11]. The temporal data quality of UAVs is usually influenced by the sensor characteristics, geometrical alignment, illumination conditions, and atmospheric conditions [12]. Consequently, it is necessary to use the reflectance rather than the digital number (DN) to better characterize the spectral properties of ground objects and

their variation through time [13]. Radiometric calibration converts the DN value to reflectance, making it possible to quantitatively analyze the data from different sensors or times [14]. However, vignetting effect and the changes in illumination conditions, exposure time, etc., can affect the image quality, resulting in differences in the radiometric properties within and between images, which poses challenges for the radiometric calibration of multiple UAV images.

There are many radiometric calibration methods for a single image. The empirical line method (ELM) is the most commonly used method [15-17], which assumes a linear transformation between DN value and surface reflectance. However, the relationship between DN value and surface reflectance is not always linear [18-20]. For example, Lei *et al.* proposed a method called the subband empirical line (SEL), which used the power transformation relation of visible light bands and the linear transformation relation of the red edge and near-infrared (NIR) bands for fitting the calibration model [19]. In addition, some other methods can also be used for converting UAV images to reflectance maps, such as Xu *et al.* presented a method called the spectral angle constraint method (SACM), which added the spectral information as a constraint to ELM for improving the calibration precision [21]. Rodriguez *et al.* utilized the parameters from the Micasense RedEdge sensor and digital light sensor (DLS) to transform DN to radiance and then used the At-Altitude Radiance Ratio (AARR) technique to obtain the surface reflectance [22], while Pines *et al.* found that the radiometric calibration accuracy of AARR was not as good as ELM when the illumination was relatively consistent or the cloud cover was low [23].

However, the radiometric calibration methods suitable for a single image may become impractical for multiple UAV images. Because during the flight of UAV, each image may be influenced by the different exposure time, different incident angle, different illumination conditions, different turbulence, or different signal processing chains [24]. As a result, there may be significant light-dark differences between images, making a

This work was supported by the Advanced Research Project of Civil Space Technology (250000815), the Dragon 5 project (UAV4VAL/ID58817), and Key R&D projects in Hubei Province (2020BBB058). (Corresponding author: Yan Gong).

Wanshan Peng, Yan Gong, Shenghui Fang, Yongjun Zhang, Jie Ren, and Jiakai Mo are with the School of Remote Sensing and Information Engineering, Wuhan University, Wuhan 430079, China (e-mail: peng_wanshan@whu.edu.cn, gongyan@whu.edu.cn, shfang@whu.edu.cn, zhangyj@whu.edu.cn, renjie2016@whu.edu.cn, wdmjcc@whu.edu.cn).

Jadunandan Dash is with the School of Geography and Environmental Science, University of Southampton, Southampton SO17 1BJ, England (e-mail: j.dash@soton.ac.uk).

> REPLACE THIS LINE WITH YOUR MANUSCRIPT ID NUMBER (DOUBLE-CLICK HERE TO EDIT) <

radiometric calibration model established on one image inappropriate for another. With the increase of UAV endurance, this problem will become more prominent. To overcome the influence of radiometric differences between UAV images, some studies have proposed methods using multiple reference targets to ensure every image contains at least one reference target [18, 25]. But it is not feasible to measure the reflectance of every reference target even in a small study area [14]. Therefore, new algorithms are needed for the radiometric calibration of multiple UAV images. Tu *et al.* used a sensor-information-based calibration method to directly generate orthomosaiced reflectance images [26], but this method did not display consistent results, probably because using only one reference target was insufficient to determine the relationship between radiance and reflectance. Further, Honkavaara *et al.* developed a radiometric calibration approach based on global optimization, which considered the impact of view/illumination geometry on the reflectance and illumination variations, and results showed that their method could improve the radiometric uniformity of the datasets [27]. Commercial software such as Pix4D (Pix4D S.A., Lucerne, Switzerland) or Photoscan (Agisoft LLC, ST. Petersburg, Russia) either directly generates the reflectance orthomosaics [28-30] or firstly generates orthomosaics, then uses ELM to radiometrically calibrate images [31-33]. Although there are many radiometric calibration methods, most of them are difficult to meet the requirements of high-precision applications [34]. Therefore, an accurate and radiometric calibration method for multiple UAV images is still a challenge.

In addition to the light-dark differences between the images, the brightness difference within an image caused by vignetting will also affect the observed values of ground objects. Vignetting is a phenomenon that refers to the radial fall-off of brightness from the image center towards the edges [35] and can be corrected by two methods: one is the polynomial fitting method [36, 37] which uses polynomial to approximate the vignetting; the other is the lookup table (LUT) method which establishes LUT by using the integration sphere [38, 39] or under homogeneous illumination conditions [40]. However, vignetting correction is challenging in practice [38], because large integration spheres are expensive, and small ones may not provide uniform illumination across the sensor's field of view (FOV) [41]. When using a Lambertian surface, due to the wide-angle lenses, it is difficult to cover the reference target completely within the FOV of sensors while obtaining homogenous illumination [42]. In addition, the above vignetting correction methods need auxiliary measurement, thereby increasing the complexity of experiments and data processing. Thus, a simple and practical method for vignetting correction would support accurate UAV data processing.

By using ground control points (GCPs) and tie points (TPs), block adjustment (BA) can effectively eliminate geometric errors [43] and be often used to correct the geometric errors of the optical satellite images [44]. In addition, some studies added different constraints to BA to improve the geometric accuracy [45]. For instance, based on an equivalent geometric sensor

model, Cao *et al.* proposed a BA method with the digital elevation model (DEM) as constraints, and the results showed that the horizontal and vertical root mean square errors (RMSEs) reduced from 17.3 m and 2.6 m to 2.5 m and 1.5 m, respectively [46]. BA first uses TPs extracted from the overlapping area of the images to establish the error equations of the geometric observations and then solves the unknown parameters by minimizing the error. In the overlapping area of images, not only the geometric information of the ground objects but also the radiometric information can be obtained. Therefore, some studies have introduced BA into the relative radiometric correction of multiple remote sensing images to eliminate the radiometric differences between images [47-49]. Further, some studies have introduced BA into the absolute radiometric calibration of satellite or UAV images. For example, Han *et al.* proposed a BA-based cross-calibration method for the images obtained by the panchromatic and multispectral sensor (PMS) on the Gaofen-4 satellite, and the results showed that the average absolute calibration relative errors range from 1.97% to 5.58% [50]. Honkavaara *et al.* proposed a BA-based radiometric calibration method that considered the influence of bidirectional reflectance distribution function (BRDF), and the results showed that the method improved the homogeneity of the datasets from 12~16% to 4~6% [51]. However, their method used only one set of parameters in each band to correct the effects of BRDF, which may affect the radiometric calibration accuracy. In addition, the position information of pixels in the image is not well utilized in the existing radiometric calibration methods based on the block adjustment.

The light-dark differences between images and the vignetting pose challenges for the radiometric calibration of multiple UAV images. However, based on the idea of BA, the radiometric and geometric information extracted from the images' overlapping areas provides an opportunity for the radiometric calibration of multiple UAV images. The objective of this paper is to achieve the radiometric calibration of multiple UAV images using only a small number of calibration blankets, thereby generating reflectance mosaics of the entire study area. To do this, we propose a radiometric block adjustment method based on the BA, which eliminates the light-dark differences between images and the vignetting inside images while the radiometric calibration. At the same time, we have designed a weight setting method to reduce the influence of view geometry and the heterogeneity of ground objects on the solution of radiometric calibration parameters. The UAV images and ground measurement data are introduced in Section II. Section III describes the radiometric block adjustment model followed by the representation of results in Section IV. Section V discusses the optimal number of control points with known reflectance, the influence of vignetting correction, uncertainties, and the potential of the proposed method. Finally, Section VI summarizes the research.

> REPLACE THIS LINE WITH YOUR MANUSCRIPT ID NUMBER (DOUBLE-CLICK HERE TO EDIT) <

II. DATA

A. Study Areas

The study areas located in Hubei Province, China, including Luojia Square of Wuhan University (114°21'19.7155"E, 30°32'15.3710"N) and Taizi Mountain of Jingshan City (112°52'18.5581"E, 30°55'24.2693"N), which were hereinafter referred to as study area 1 and study area 2, respectively, as shown in Fig. 1. Study area 1 mainly included lawns, buildings, and roads, and the ground objects of study area 2 had much larger variation including forest, water, roads, soil, and buildings. Eight 1.2 m × 1.2 m calibration blankets made with highly durable woven polyester fabric (the reflectance was 0.03, 0.06, 0.12, 0.24, 0.36, 0.48, 0.56, and 0.80) were placed in the centers of the two study areas. According to the radiation characteristics of the ground objects in the two study areas and the quality of UAV images, the blankets with reflectance between 0.03~0.24 were only used in the next experiments.

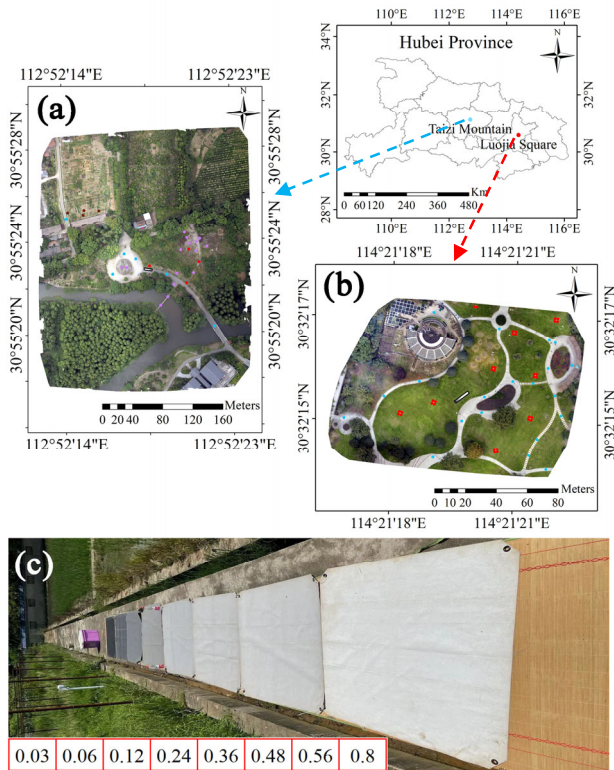


Fig. 1. Study areas. (a) Taizi Mountain, (b) Luojia Square and (c) radiometric blankets. The dots in the figure are the ground samples. The red and blue dots represent the vegetation and road, the brown dots are soil and the purple are other ground objects, such as sand. The positions of the calibration blankets are marked by black frames. The numbers in the red box in figure (c) are the reflectance of the corresponding calibration blankets.

B. Data Acquisition

P4 Multispectral (DJI, Shenzhen, China. Hereinafter referred to as P4) was used to obtain images from the two study areas. P4 integrates 6 COMS sensors including one red-green-blue (RGB) sensor for visible light imaging and five monochrome sensors for multispectral imaging. The bands of multispectral cameras are blue (B, 450 ± 16 nm), green (G, 560 ± 16 nm), red (R, 650 ± 16 nm), red edge (RE, 730 ± 16 nm), and NIR (840 ±

26 nm). The cameras' FOV is 62.7°, the max image size is 1600×1300, and the focal length is 5.74 mm.

DJI GS PRO (DJI, Shenzhen, China) was used to plan the flight path, and the settings are shown in TABLE I. The exposure mode was set to auto to allow the sensors to gather light information and timely adjusted the exposure time. Therefore, even if the images came from the same camera, their exposure time might be different. In total 606 images for study area 1 were collected under clear weather conditions, whereas, 1566 images were collected for study area 2, but under cloudy condition causing obvious radiometric differences between images.

TABLE I
FLIGHT SETTINGS. GSD: GROUND SAMPLING DISTANCE

Study Area	Luojia Square	Taizi Mountain
Date (UTC+8)	2020.12.19 12:33-13:13	2021.06.08 13:47-14:24
Shooting Mode	Hover	Hover
Altitude (m)	50	100
GSD (cm)	2.56	5.29
Forward/Side overlap (%)	80/60	80/80

The ASD FieldSpec 4 (ASD Inc., Boulder, CO, USA) spectrometer was used to measure the spectra of ground samples during the flight mission. Before each measurement, the ASD was calibrated using a calibrated white reference. In study area 1, each ground sample was measured once, and 5 spectra were obtained, then the average of the 5 spectra was taken as the spectrum of the ground sample. In study area 2, the same measurement method as study area 1 was used, but the only difference was that each ground sample was measured three times. The ASD measurements were then converted to spectral reflectance using ViewSpecPro software and exported to the text files. Finally, 54 samples were obtained in study area 1, including 34 vegetation and 20 road samples; 29 samples were obtained in study area 2, including 4 vegetation, 6 road, 4 soil, and 15 other categories of samples. All ground samples were used to evaluate the accuracy of the radiometric calibration.

As the spectral response functions (SRFs) of P4 were unknown, the Gaussian function, central wavelength, and full width at half maxima (FWHM) were used to simulate these functions in this paper. Then the spectra of ground samples were resampled, and the equation of resampling is given as follows:

$$\rho_i = \int_{\lambda_1}^{\lambda_2} \rho_\lambda S_\lambda d\lambda / \int_{\lambda_1}^{\lambda_2} S_\lambda d\lambda, \quad (1)$$

where ρ_λ is the reflectance at the wavelength λ , S_λ is the simulated spectral response at the wavelength λ , $[\lambda_1, \lambda_2]$ is the wavelength range of the i th band of the P4, and ρ_i is the equivalent reflectance for the i th band.

III. METHODOLOGY

A. Radiometric Block Adjustment Model

Reflectance is an intrinsic property of ground objects. In other words, the reflectance of the same ground object should

> REPLACE THIS LINE WITH YOUR MANUSCRIPT ID NUMBER (DOUBLE-CLICK HERE TO EDIT) <

be equal on all images after radiometric calibration. If there are some ground points with known reflectance, all UAV images of the study area can be radiometrically calibrated by using the information from overlapping areas of images. Before introducing the radiometric block adjustment model, we define the two key concepts of radiometric control points (RCPs) and radiometric tie points (RTPs). RTPs are ground objects with multiple geometric and radiometric observations, and RCPs are ground objects with known reflectance.

In this paper, we adopt SEL to describe the relationship between DN value and surface reflectance because in visible light bands, using power transformation will obtain higher fitting accuracy than linear transformation [19]. In addition, using the power transformation can avoid the situation where the calculated reflectance of the low reflectance regions is negative. The SEL model is as follows:

$$DN = a\rho + b, \quad (2)$$

$$DN = b\rho^a, \quad (3)$$

where ρ is the reflectance, a and b are the absolute correction coefficients. Equation (2) is suitable for the RE and NIR bands, and (3) is suitable for the visible light bands.

Using one image as the reference (i.e. the reference image), radiometric differences between images can be eliminated by adjusting the radiation levels of other images to be consistent with it. A common and effective way to eliminate radiometric differences between images is to assume a linear transformation relationship between images [27, 52]. The reference image should contain calibration blankets to provide initial values for absolute calibration parameters. In addition, the calibration blankets should be located in the center of the reference image as much as possible to reduce the effect of vignetting on the initial values of absolute calibration parameters. After selecting the reference image, the relationship between the reflectance $\rho_{RTP,j}$ of RTP j in image i and its DN can be described as follows:

$$DN_{ij} = a_i(a\rho_{RTP,j} + b) + b_i, \quad (4)$$

$$DN_{ij} = a_i b \rho_{RTP,j}^a + b_i, \quad (5)$$

where DN_{ij} is the DN value of RTP j in image i , a_i and b_i are the relative calibration coefficients. Theoretically, (4) and (5) realize the unification of absolute and relative radiometric calibration.

Since vignetting is highly correlated with pixel position, it can be expressed as a function of pixel position. Based on the characteristic that vignetting gradually reduces the brightness of the image from the center to the edges, we use the following paraboloid model to correct vignetting:

$$V(u,v) = p_0 + p_1 u^2 + p_2 v^2, \quad p_0, p_1, p_2 > 0, \quad (6)$$

where p_0, p_1 and p_2 are the paraboloid parameters, (u,v) is the pixel coordinate system established with the image center as the origin, and $V(u,v)$ is the vignetting correction factor at (u,v) . Because of the imperfect manufacturing process, the brightness center is usually inconsistent with the image center [38]. Taking this into account, precise compensation of the vignetting effect can be achieved by moving it from the image center to the

brightness center, assuming that the shape of the paraboloid remains constant. Then (6) becomes

$$\begin{aligned} V(u,v) &= p_0 + p_1(u-u_0)^2 + p_2(v-v_0)^2 \\ &= p_1 u^2 + p_2 v^2 - 2p_1 u_0 u - 2p_2 v_0 v + p_1 u_0^2 + p_2 v_0^2 + p_0 \quad (7) \\ &= p_1 u^2 + p_2 v^2 + p_3 u + p_4 v + p_5, \end{aligned}$$

where

$$\begin{aligned} p_3 &= -2p_1 u_0, \\ p_4 &= -2p_2 v_0, \end{aligned} \quad (8)$$

$$p_5 = p_1 u_0^2 + p_2 v_0^2 + p_0,$$

where (u_0, v_0) is the translation parameter from the image center to the brightness center. The proposed method has some noise immunity, and the dark current can be regarded as noise to some extent, so we did not perform the dark current correction when processing the data. However, the parameter p_5 has a very significant influence on the solution of the model. To ensure the rationality of the solutions of radiometric calibration parameters, the value of the parameter p_5 must be limited. At the vignetting center, if the dark current is DC , the DN value is DN_0 , the vignetting correction parameter is p_5 , then we have

$$DN_0 \cdot p_5 = DN_0 - DC. \quad (9)$$

So, the value of p_5 is

$$p_5 = 1 - DC / DN_0. \quad (10)$$

The dark current generally is small and in this paper, we assume that the maximum value of dark current will not exceed 10% of the maximum DN value (e.g. the maximum value of a 16-bit image is 65535). To estimate the value of p_5 , the average DN of the image center in a 99×99 window is used instead of DN_0 . For every image, p_5 has an estimation value and then the 70th percentile of all estimation values, $p_{5,70}$, will be set as the low limitation of p_5 , i.e.

$$p_5 \geq p_{5,70}. \quad (11)$$

Finally, we can describe the relationship between the DN value of RTP j in image i and its reflectance as:

$$(p_1 u^2 + p_2 v^2 + p_3 u + p_4 v + p_5) DN_{ij} = a_i (a \rho_{RTP,j} + b) + b_i, \quad (12)$$

$$(p_1 u^2 + p_2 v^2 + p_3 u + p_4 v + p_5) DN_{ij} = a_i b \rho_{RTP,j}^a + b_i. \quad (13)$$

Since the theoretical derivation of the radiometric block adjustment model under the linear transformation and power transformation is similar, here only the linear transformation is used as an example to derive the model. The error equation of RTP j in image i is as follows:

$$v_{ij} = a_i (a \rho_{RTP,j} + b) + b_i - (p_1 u^2 + p_2 v^2 + p_3 u + p_4 v + p_5) DN_{ij}, \quad w_{ij}, \quad (14)$$

where w_{ij} is the weight, and v_{ij} is the error. Equation (14) is a nonlinear equation that is difficult to solve. To facilitate the solution, we use Taylor Formula to linearize the error equation as follows:

> REPLACE THIS LINE WITH YOUR MANUSCRIPT ID NUMBER (DOUBLE-CLICK HERE TO EDIT) <

$$V = Ax - L, \quad W, \quad (23)$$

$$v_{ij} = v_{ij}^0 + \frac{\partial v_{ij}}{\partial a} \Delta a + \frac{\partial v_{ij}}{\partial b} \Delta b + \frac{\partial v_{ij}}{\partial a_i} \Delta a_i + \frac{\partial v_{ij}}{\partial b_i} \Delta b_i + \frac{\partial v_{ij}}{\partial \rho_{RTP,j}} \Delta \rho_{RTP,j} \\ + \frac{\partial v_{ij}}{\partial p_1} \Delta p_1 + \frac{\partial v_{ij}}{\partial p_2} \Delta p_2 + \frac{\partial v_{ij}}{\partial p_3} \Delta p_3 + \frac{\partial v_{ij}}{\partial p_4} \Delta p_4 + \frac{\partial v_{ij}}{\partial p_5} \Delta p_5, \quad (15)$$

where v_{ij}^0 is the value obtained by substituting the results of the previous iteration of the unknown parameters into (14) and the partial derivative are as follows:

$$\frac{\partial v_{ij}}{\partial a} = a_i \rho_{RTP,j}, \quad \frac{\partial v_{ij}}{\partial b} = a_i, \quad \frac{\partial v_{ij}}{\partial \rho_{RTP,j}} = a_i a, \quad \frac{\partial v_{ij}}{\partial b_i} = 1 \\ \frac{\partial v_{ij}}{\partial a_i} = a \rho_{RTP,j} + b, \quad \frac{\partial v_{ij}}{\partial p_1} = -u^2 DN_{ij}, \quad \frac{\partial v_{ij}}{\partial p_2} = -v^2 DN_{ij}, \quad (16) \\ \frac{\partial v_{ij}}{\partial p_3} = -u DN_{ij}, \quad \frac{\partial v_{ij}}{\partial p_4} = -v DN_{ij}, \quad \frac{\partial v_{ij}}{\partial p_5} = -DN_{ij}.$$

RCPs (i.e. calibration blankets) are added as constraints to the model. If the true reflectance of RCP k is $\rho_{RCP,k}$ and the reflectance calculated in the iterative process is $\rho'_{RCP,k}$, the error equation is as follows:

$$v_{RCP,k} = \rho'_{RCP,k} - \rho_{RCP,k}, \quad w_{RCP}, \quad (17)$$

where w_{RCP} is the weight. For the reference image, its relative calibration coefficients are 1 and 0 respectively, so their error equations are as follows:

$$\begin{cases} v_{ref,a} = a_{ref} - 1, & w_{ref} \\ v_{ref,b} = b_{ref} - 0, & w_{ref} \end{cases}, \quad (18)$$

where a_{ref} and b_{ref} are the calculated values of relative calibration coefficients of the reference image, and w_{ref} is the weight.

In this paper, the ranges of absolute calibration coefficients a and b are limited for ensuring the reasonability of solving the equation. If the initial value of a and b calculated by using the calibration blankets are a_{ini} and b_{ini} , and the calculated value are a_{cal} and b_{cal} , then the error equation of a and b are as follows:

$$v_a = a_{cal} - a_{ini}, \quad w_{abs}, \quad (19)$$

$$v_b = b_{cal} - b_{ini}, \quad w_{abs}, \quad (20)$$

where w_{abs} is the weight.

Generally speaking, although the vignetting center is often not consistent with the image center, the two are not too far apart, i.e. the (u_0, v_0) is small. Based on this reason, p_3 and p_4 are limited as follows:

$$\begin{cases} v_{p_3} = p'_3 - 0, \\ v_{p_4} = p'_4 - 0, \end{cases} \quad w_p, \quad (21)$$

where p'_3 and p'_4 are iteration results, w_p is the weight.

To improve the efficiency of solving equations, we limit the range of some parameters as follows:

$$\rho_{RTP,j}, \rho_{RCP,k} \in [0, 1], \\ a_i \geq 0, \\ a \geq 0. \quad (22)$$

In summary, we can describe the radiometric block adjustment model in the form of matrices as follows:

where V is the residual vector, A is the design matrix including the partial derivative of unknown parameters and the coefficients of control equations, x is the vector consisting of the increments of the unknown parameters, L is the vector of observations, and W is the weight matrix. The x can be solved by minimizing the residuals. The solution of unknown parameters is an iterative process. When the solution of x is less than 10^{-6} or the iteration is over 500 times, the iteration is stopped, and the output is the solution of the unknowns. For ease of solving, the DN values are scaled to 0~1 (based on the bit-depth of UAV images), while pixel coordinates are scaled to -1~1 (based on the image size).

The unknown parameters of the radiometric block adjustment model are listed as follows:

- 1) Absolute calibration parameters: a and b , which are used to convert DN value to reflectance;
- 2) Relatively calibration parameters: a_i and b_i ($i=1, 2, \dots, c$, c is the number of images), which are used to eliminate the light-dark differences between images.
- 3) Vignetting correction parameters: p_m ($m=1, 2, \dots, 5$);
- 4) The reflectance of RTP: $\rho_{RTP,j}$ ($j=1, 2, \dots, N$, N is the number of RTPs);
- 5) The reflectance of RCP: $\rho_{RCP,k}$ ($k=1, 2, \dots, K$, K is the number of RTPs), which is used as constraint condition.

B. Weight Settings

The weights are an assessment of the reliability of the observations. In generally, RTPs should be homogeneous. However, the flight altitude of UAV is usually low, so the ground objects will have more details, which increases the difficulty of finding uniform ground objects. To reduce the effect of ground objects' non-uniformity on solution results of radiometric calibration parameters, we use the purity of the ground objects to determine the weights of error equations. The purity of RTP j in image i is defined as follows:

$$p_{ij} = \sigma_{ij} / avg_{ij}, \quad (24)$$

where σ_{ij} and avg_{ij} are the standard deviation and average of the DN values within a window centered on RTP j . And the weight of RTP j is calculated by the following equation:

$$w_{ij}^1 = \exp(-3 p_{ij}), \quad (25)$$

where the constant 3 is used to expand the differences between the weights.

In addition, the reflectance of a ground object will change with the changes of view geometry, i.e. BRDF effect. In general, reflectance will reach a maximum at the hot-spot, and be more stable away from the hot spot. To reduce the influence of view geometry, we assign a smaller weight to RTP close to the hot-spot and a larger weight to RTP far away from the hot-spot, and the weight is calculated as follows:

$$w_{ij}^2 = -\exp(-(\theta_{v,ij} - \theta_{s,i})^2 / (2\sigma_{v,i}^2)) + 1.005, \quad (26)$$

where $\theta_{s,i}$ is the solar zenith angle when collected the image i , $\theta_{v,ij}$ is the view zenith angle of the RTP j in image i , and $\sigma_{v,i}$ is defined as follows:

> REPLACE THIS LINE WITH YOUR MANUSCRIPT ID NUMBER (DOUBLE-CLICK HERE TO EDIT) <

$$\sigma_{v,i} = \sqrt{\frac{1}{n} \sum_j (\theta_{v,ij} - \theta_{s,i})^2}. \quad (27)$$

where n is the number of RTPs on image i . Finally, the weight of the error equation can be set as follows:

$$w_{ij} = w_{ij}^1 \cdot w_{ij}^2. \quad (28)$$

This weight setting method can reduce the influence of heterogeneity of ground objects and the view geometry. The reflectance of RCPs and the relative calibration parameters of the reference image are also solved as unknowns. In fact, their values are known. To ensure the accuracy of their solutions, a larger weight should be given to (17) and (18) as follows:

$$w_{RCP}, w_{ref} = 100. \quad (29)$$

The power function is more complex than the linear function. If the absolute calibration parameters of power transformation are not limited, there may be no solution or the solution may be unreasonable; contrary to this, the linear transformation is relatively simple, and this situation will not happen. Therefore, we set different values for w_{abs} as follows:

$$w_{abs} = \begin{cases} \max(\mathbf{w}), & \text{power transformation} \\ 0, & \text{linear transformation} \end{cases}, \quad (30)$$

where \mathbf{w} is the set consisting of the weights of all RTPs.

In general, the vignetting center is close to the image center. However, the solution of parameters p_3 and p_4 will be affected by many factors, such as the BRDF, the types of ground objects, etc. To reduce the influence of these factors, we set the weight of (21) slightly larger as follows:

$$w_p = 10 \max(\mathbf{w}). \quad (31)$$

C. Data Processing

Firstly, the UAV images were processed by Pix4D. The outputs included interior orientation parameters (IOP) of each sensor, exterior orientation parameters (EOP) of each image, lenses distortion correction parameters, the transformation matrix to convert the ground coordinates to pixel coordinates, DSMs and orthomosaics. The P4 multispectral images, the coordinates of RCPs and their reflectance, and those above-mentioned outputs of Pix4D were used as inputs of the radiometric block adjustment. Each band was processed separately. Reflectance mosaics were then generated using the calibration parameters output from the radiometric block adjustment. The rules of generating reflectance mosaics were as follows: the reflectance of a ground point in the mosaic was the value that had the most nadir geometry [51].

As the bridge between images, RTPs play a very important role in the radiometric block adjustment. When selecting RTPs, the number of them on each image should not be too small, otherwise, the redundant observations are not enough to solve the optimal radiometric calibration parameters. On the contrary, the number of RTPs should not be too many because it will make the number of error equations increase sharply and reduce the efficiency of solving. In this paper, RTPs were selected from the DSM at fixed intervals, as shown in Fig. 2. Ideally, there were up to 100 RTPs on a UAV image. The average value in a 17×17 window was calculated to take it as the DN value of an RTP. In addition, RTPs that appeared less than 3 times were

removed to avoid too many unknown parameters.

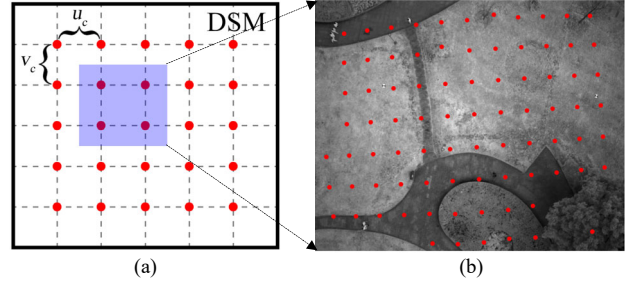


Fig. 2. Examples of (a) selection of RTPs from DSM. The parameters u_c and v_c are the intervals determined by the UAV image size and (b) distribution of RTPs on a UAV image. The red dots are the selected RTPs.

D. Performance Assessment

The performance of the proposed method in this paper was evaluated in terms of visual and quantitative perspectives. Visual assessment was mainly based on the homogeneity of reflectance mosaics. The quantitative assessment included two parts: one was the change in the internal uniformity of the dataset before and after processing, and the other was to assess the radiometric calibration accuracy using ground samples. The internal uniformity of the dataset was evaluated using the coefficient of variation (CV) and its definition was as follows:

$$CV_j = 100 \frac{\sigma_{RTP,j}}{avg_{RTP,j}}, \quad (32)$$

where $avg_{RTP,j}$ and $\sigma_{RTP,j}$ are the average and standard deviation of DN of RTP j respectively. The average CV of all RTPs was used to represent the internal uniformity of the dataset. The CV calculated with DN could reflect the quality of the relative calibration to some extent, while the CV using reflectance could reflect the quality of the absolute calibration. Thus, except for the CV calculated using DN, the CV calculated using reflectance was also used for evaluating the internal uniformity of the dataset, and they were referred to below as CV_{DN} and CV_{ref} , respectively.

Two indicators, RMSE and Mean Relative Percent Error (MRPE), were also used to evaluate the calibration accuracy, and their definitions were as follows:

$$RMSE = \sqrt{\frac{1}{N} \sum_{i=1}^N (\rho_{cal,i} - \rho_{ASD,i})^2}, \quad (33)$$

$$MRPE = \frac{1}{N} \sum_{i=1}^N \left| 100 \times \frac{\rho_{cal,i} - \rho_{ASD,i}}{\rho_{ASD,i}} \right|, \quad (34)$$

where N is the number of samples, $\rho_{cal,i}$ is the predicted reflectance, and $\rho_{ASD,i}$ is the reflectance of ground samples.

To better analyze the performance of the proposed method, three other methods were used for comparison: (1) Direct Mosaic, where mosaics were generated directly using original images and then calibrated with SEL; (2) Blending, where the orthomosaics were output by PhotoScan and then calibrated with SEL; (3) Color Balancing, where the orthomosaics were output by Pix4D and the reflectance maps were generated by SEL. For convenience, the method proposed in this paper was referred as RBA in the following.

> REPLACE THIS LINE WITH YOUR MANUSCRIPT ID NUMBER (DOUBLE-CLICK HERE TO EDIT) <

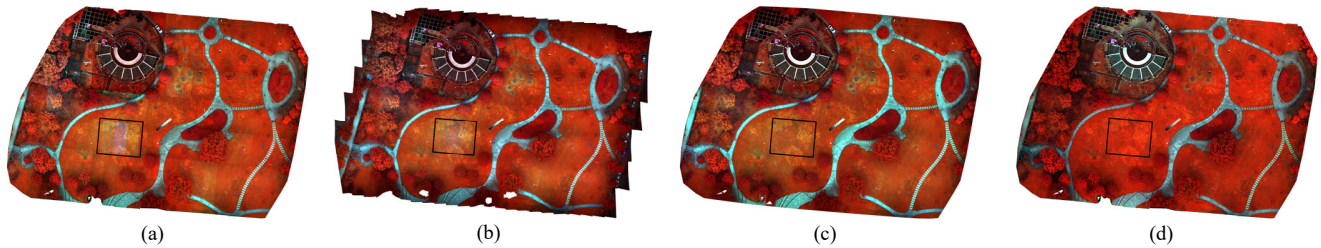


Fig. 3. Color infrared mosaics of study area 1 with NIR, green and blue bands. (a) Direct Mosaic, (b) Blending, (c) Color Balancing, and (d) RBA.

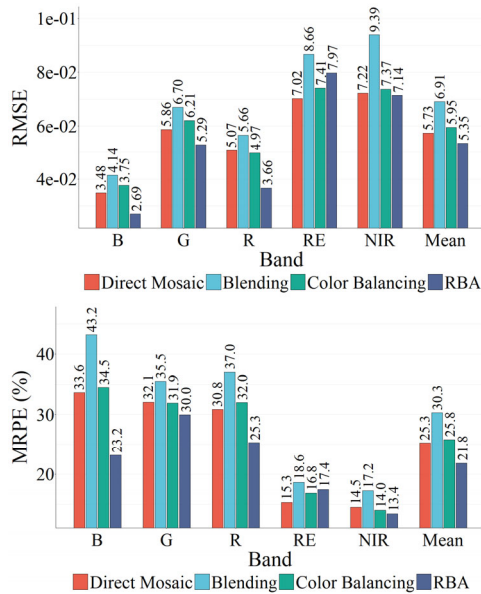


Fig. 4. Calibration accuracy of study area 1. Mean: the average of all bands.

TABLE II
CV(%) OF STUDY AREA 1

	CV _{DN}		CV _{ref}	
	Direct Mosaic	RBA	Direct Mosaic	RBA
B	17.9	5.6	25.9	8.2
G	16.4	5.1	22.5	7.5
R	16.8	5.9	22.2	8.1
RE	13.9	4.7	23.0	7.9
NIR	12.9	5.2	19.5	8.2

IV. RESULTS

A. Results of Radiometric Calibration

Fig. 3 shows the reflectance mosaics of study area 1 generated by the four methods. Due to the variation in illumination, exposure time, etc., there are varying degrees of difference in the brightness of the original images, so the patches and seamline can be seen in Fig. 3 (a). Blending, Color Balancing, and RBA could eliminate the radiometric differences and generate mosaics with good visual quality, as shown in Fig. 3 (b), (c), and (d). However, the mosaics of different methods differ in detail, as shown in the black box in Fig. 3, which was related to the method of relative radiometric calibration and generating mosaics.

Fig. 4 is the calibration accuracy of different methods in study area 1. In the visible light and NIR bands, RBA obtained the best results compared to the other three methods, with

RMSE and MRPE ranging from 0.027 to 0.071 and 13.4% to 30.0%, respectively. For the RE band, Direct Mosaic had the best accuracy with RMSE and MRPE of 0.070 and 15.3%, respectively. On the whole, RBA was the best of all four methods, with mean RMSE and MRPE of 0.054 and 21.8%, respectively.

TABLE II is the CV of study area 1. Because the process of generating orthomosaics in PhotoScan and Pix4D was unknown, the CV of Blending and Color Balancing was not calculated. Compared with the Direct Mosaic, the CV_{DN} of RBA reduced above 10.5% in visible light bands and about 8.0% in RE and NIR bands. Similarly, CV_{ref} was significantly reduced. Among them, the CV_{ref} in the blue band had the most decrease, about 17.7%, and the NIR band had the least decrease, but it also had 11.3%.

Due to the influence of clouds, the illumination changes in study area 2 were severe. In this case, we did not consider the effect of BRDF on sensors' observations. Therefore, (25) was used instead of (28) to determine the weights of error equations established by RTPs. Reflectance mosaics of study area 2 are shown in Fig. 5. The color of the upper left part of the mosaics generated by all four methods was different from other parts of the mosaics because, in the blue band, there was an obvious overexposure phenomenon in the raw data in this region. And this problem also appeared in the red band. There were obvious color differences in Fig. 5 (a), which indicated the original images had significant light-dark differences. Blending, Color Balancing and RBA improved the uniformity of the reflectance mosaics (Fig. 5 (b), (c) and (c)). But in Fig. 5 (b) and (c), the color of the mosaic center was different from the around. Furthermore, the outermost parts of the images in Fig. 5 (b) and (c) were darker than the rest. This phenomenon could also be found in Fig. 3 (b) and (c), but was not as pronounced as in Fig. 5 (b). The reason for this phenomenon may be that the vignetting was not fully corrected. Overall, RBA could generate the mosaic with the best visual quality among all four methods.

Fig. 6 shows the calibration accuracy of study area 2. In visible light bands, RBA had the best performance, with RMSE of 0.031~0.035 and MRPE of 19.6%~27.1%. The results of Direct Mosaic and Blending were close and the least accurate among all methods, with RMSE and MRPE of 0.064~0.105 and 46.2%~64.3%, respectively. In the RE band, Blending had the best accuracy, with RMSE and MRPE of 0.035 and 16.5%, respectively; in the NIR band, the calibration accuracy of Color Balancing was the highest, with RMSE and MRPE of 0.044 and 15.5%, respectively. Similar to the experimental results of study

> REPLACE THIS LINE WITH YOUR MANUSCRIPT ID NUMBER (DOUBLE-CLICK HERE TO EDIT) <

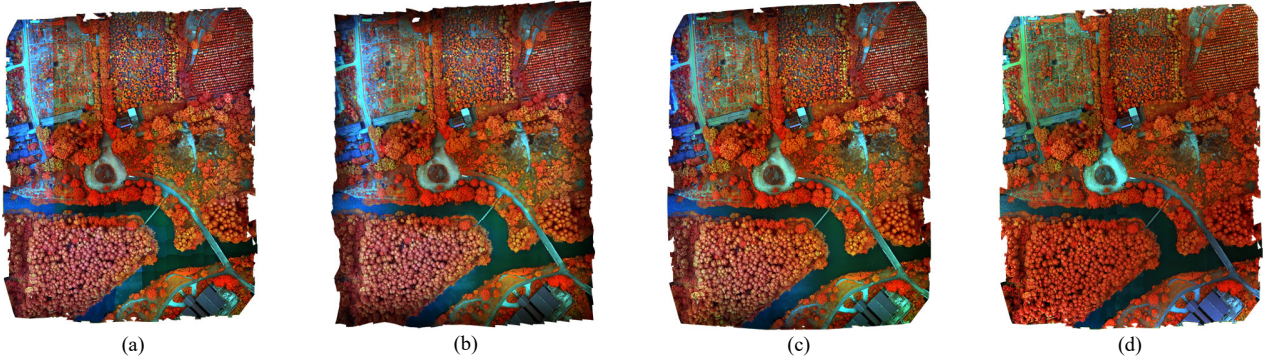


Fig. 5. Color infrared mosaics of study area 2 with NIR, green and blue bands. (a) Direct Mosaic, (b) Blending, (c) Color Balancing, and (d) RBA.

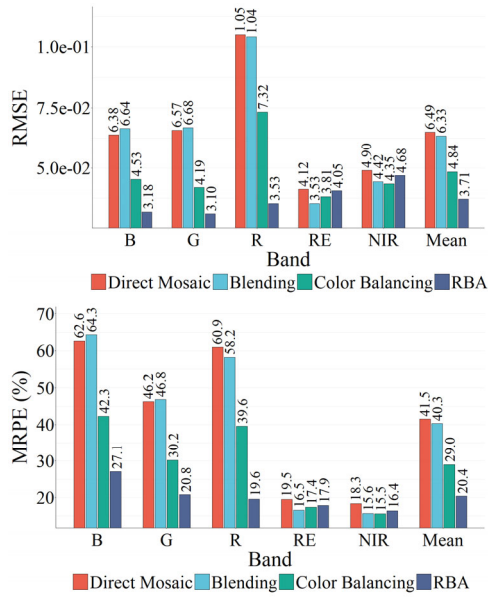


Fig. 6. Calibration accuracy of study area 2. Mean: the average of all bands.

TABLE III
CV(%) OF STUDY AREA 2

	CV _{DN}		CV _{ref}	
	Direct Mosaic	RBA	Direct Mosaic	RBA
B	20.4	13.3	37.3	20.5
G	17.2	12.0	27.5	16.7
R	22.5	14.4	34.4	19.1
RE	15.5	9.9	28.2	18.4
NIR	14.5	10.4	24.7	18.9

area 1, RBA could significantly improve the calibration accuracy in visible light bands, but its performance in RE and NIR bands was similar to the other three methods.

TABLE III is the CV of study area 2. RBA significantly increased the uniformity between images, and the reduction range of CV_{DN} was between 4.1% and 8.1% compared with Direct Mosaic. Similarly, the CV_{ref} decreased significantly and among them, the CV_{ref} of the blue band decreased the most, reaching 16.7%, while the CV_{ref} of the NIR band decreased the least, being 5.8%. The results in TABLE II and TABLE III showed that the RBA could effectively reduce the radiometric differences and improve the uniformity of datasets.

TABLE IV

THE RMSE AND MRPE OBTAINED BY USING 4 CALIBRATION BLANKETS AND 5-FOLD CROSS-VALIDATION IN STUDY AREA 1

	RMSE ($\times 10^{-2}$)		MRPE (%)	
	4 calibration blankets	5-fold cross-validation	4 calibration blankets	5-fold cross-validation
B	2.69	1.85	23.2	17.7
G	5.29	2.99	30.0	14.4
R	3.66	2.35	25.3	15.6
RE	7.97	6.08	17.4	16.0
NIR	7.14	6.43	13.4	13.3
Mean	5.35	3.94	21.8	15.4

TABLE V

THE RMSE AND MRPE OBTAINED BY USING 4 CALIBRATION BLANKETS AND 5-FOLD CROSS-VALIDATION IN STUDY AREA 2

	RMSE ($\times 10^{-2}$)		MRPE (%)	
	4 calibration blankets	5-fold cross-validation	4 calibration blankets	5-fold cross-validation
B	3.18	2.31	27.1	20.8
G	3.10	2.16	20.8	14.8
R	3.53	2.94	19.6	17.8
RE	4.05	3.50	17.9	16.0
NIR	4.68	4.47	16.4	16.4
Mean	3.71	3.07	20.4	17.2

B. Influences of the Number of RCPs on Radiometric Block Adjustment

From a practical point of view, only using the calibration blankets is convenient and effortless. However, from the perspective of model verification, it is not comprehensive enough to use only the calibration blankets as RCPs. One is that the number of RCPs is small; and the other is that the calibration blankets are placed centrally in the study areas, which means the distribution of RCPs is limited in the study area. These two factors will influence the error propagation and accumulation during the adjustment, thereby affecting the calibration accuracy of RBA. For this reason, 5-fold cross-validation was used to evaluate the calibration accuracy for comprehensively understanding the performance of RBA, and the Direct Mosaic, Blending, and Color Balancing were still used as the comparison methods. The 5-fold cross-validation divided the ground samples into 5 groups on average. Each time, one group was used as the validation samples, and the remaining 4 groups were used as the modeling samples. Repeated 5 times and used the mean RMSE and MRPE as the final validation results.

> REPLACE THIS LINE WITH YOUR MANUSCRIPT ID NUMBER (DOUBLE-CLICK HERE TO EDIT) <

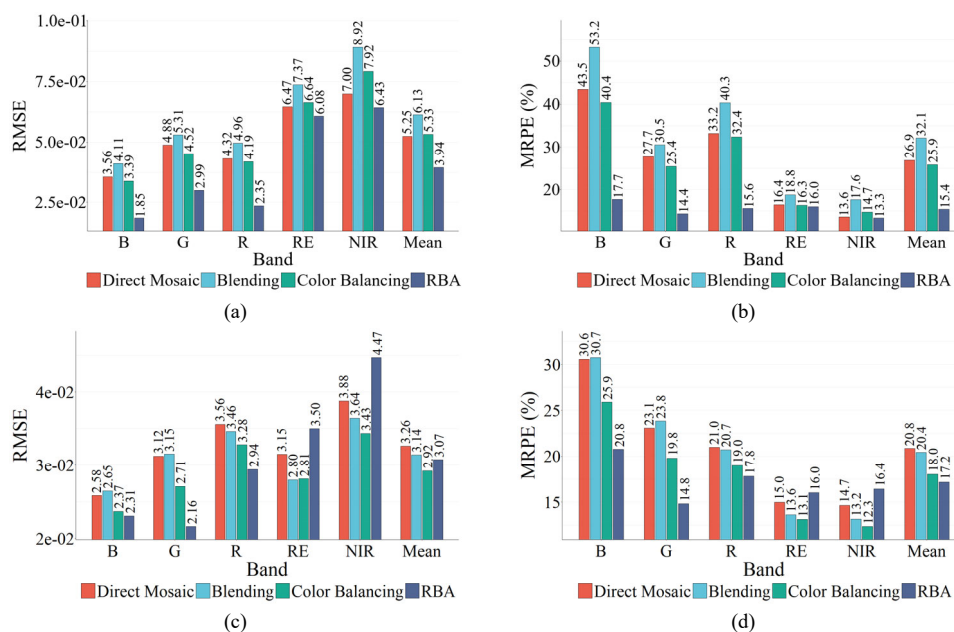


Fig. 7. The results of 5-fold cross-validation. (a) and (b) are the results of study area 1, (c) and (d) are the results of study area 2. Mean: the average of all bands.

Furthermore, to provide good initial values for the absolute calibration parameters, calibration blankets were used in each modeling process.

Fig. 7 shows the 5-fold cross-validation results. The results of the two study areas showed that RBA had the best calibration accuracy in the visible light bands, and the range of RMSE and MRPE was 0.019~0.030 and 14.4%~20.8% respectively. In RE and NIR bands, RBA had the best calibration accuracy in study area 1, with RMSE of 0.061 and 0.064, and MRPE of 16.0% and 13.3%; but in study area 2, Color Balancing got the highest calibration accuracy (except for the RMSE of the RE band), with RMSE and MRPE of 0.028, 13.1%, and 0.034, 12.3%, respectively.

TABLE IV and TABLE V show the results of using only the calibration blankets as RCPs and 5-fold cross-validation. In the two study areas, except for the MRPE in the NIR band of study area 2, the results of 5-fold cross-validation were better than the results of using only the calibration blankets as RCPs. The RMSE was reduced by 0.006~0.023 in visible light bands, and the MRPE was reduced by 1.8%~15.6%, while in RE and NIR bands, the ranges of reduced RMSE and MRPE were 0.002~0.019 and 0.0%~1.9%. These results demonstrated that the error propagation and accumulation were effectively controlled by adding RCPs.

V. DISCUSSION

A. Optimal number of RCPs

After adding RCPs, the radiometric calibration accuracy of RBA could improve prominently. In practice, it is impossible to add too many RCPs because it will significantly increase the workload. In this part, the ground samples of study area 1 were divided into vegetation and non-vegetation, and a pair of such samples were added to RBA each time to explore the optimal number of RCPs. Considering the distribution of RCPs and the error propagation and accumulation, the ground samples

located in the four corners were selected firstly. Fig. 8 shows that RMSE and MRPE decrease with the increasing number of RCPs. Adding more RCPs only slightly improves the calibration accuracy compared to the result of adding 2 pairs of RCPs. The further away from the RCPs, the more pronounced the error propagation and accumulation will be. When adding 1 RCP to each of the 4 corners of the study area, the error propagation and accumulation could be effectively controlled in the whole range; therefore, the improvement in calibration accuracy is relatively limited by adding more RCPs. Thus, adding one ground sample in each of the four corners of the study area is a reasonable choice that can not only improve the calibration accuracy but also control the workload to an appropriate level.

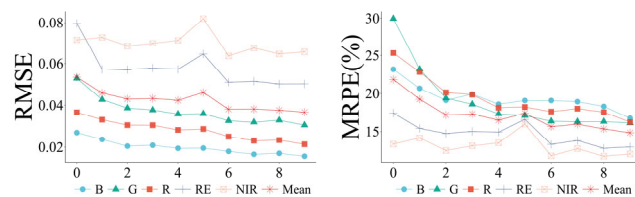


Fig. 8. The trends of RMSE and MRPE with adding the vegetation and non-vegetation ground samples as RCPs. Abscissa represented the number of RCP pairs, and 0 represented the situation using only calibration blankets as RCPs.

B. Influences of Vignetting Correction on Radiometric Block Adjustment

In general, vignetting correction is performed prior to the radiometric calibration [53]. However, the RBA proposed in this paper corrects the vignetting at the same time as the radiometric calibration. For understanding the influences of vignetting correction on RBA, another two ways were used to process the data: one was that directly used the models described by (4) and (5) to calibrate images, and the second was that the dark current and vignetting were corrected firstly and then the (4) and (5) were used to calibrate images. The dark

> REPLACE THIS LINE WITH YOUR MANUSCRIPT ID NUMBER (DOUBLE-CLICK HERE TO EDIT) <

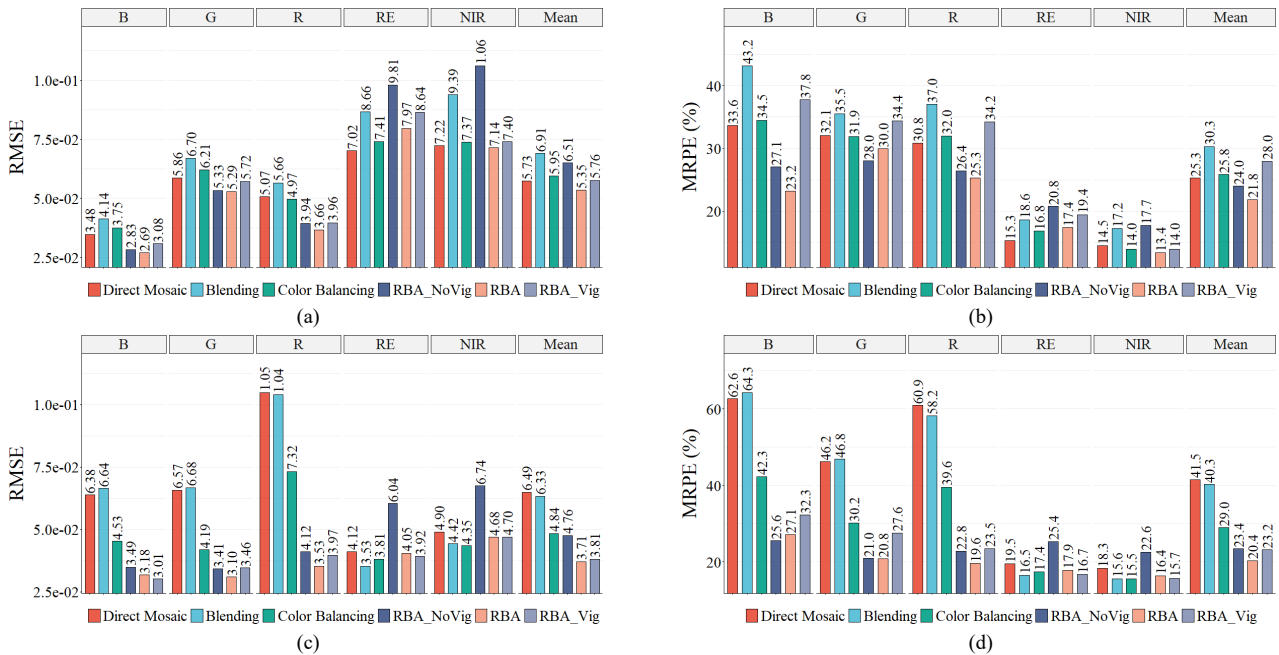


Fig. 9. Radiometric calibration accuracy of different methods when only the calibration blankets were used as RCPs. (a) and (b) are the results of study area 1, (c) and (d) are the results of study area 2. Mean: the average of all bands.

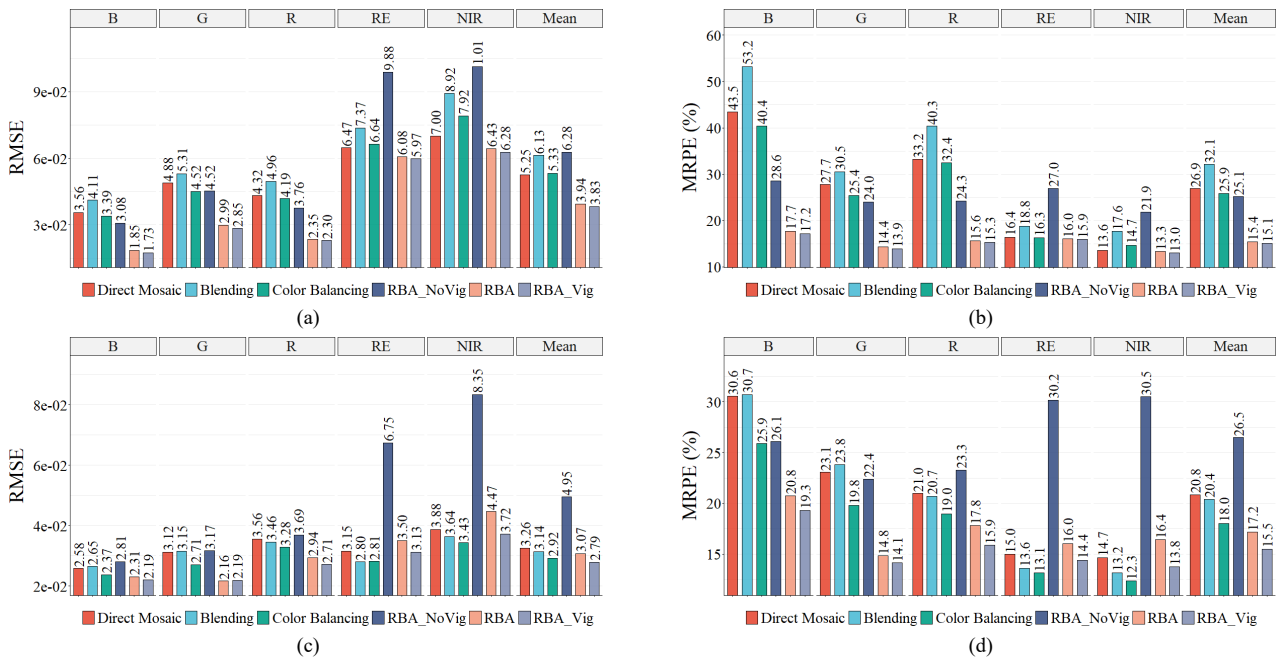


Fig. 10. The 5-fold cross-validation results of different methods in study area 1. (a) and (b) are the results of study area 1, (c) and (d) are the results of study area 2. Mean: the average of all bands.

current and vignetting correction parameters were extracted from the XMP information of images, and the detailed information could be found in the P4 image processing guide (please see: <https://www.dji.com/p4-multispectral/downloads>). These two methods were called RBA_NoVig and RBA_Vig in the following.

Fig. 9 shows results of the two study areas when only using calibration blankets as RCPs. In visible light bands, the RMSE and MRPE of RBA were the lowest for all six methods (except for the RMSE of the B band in study area 2), with RMSE of

0.027~0.053 and MRPE of 19.6~30.0%; the results of RBA_NoVig were better than the results of Direct Mosaic, Blending, and Color Balancing, which indicates that the RBA_NoVig had a certain ability to correct vignetting. For RE and NIR bands, different methods had different performance. In study area 1, Direct Mosaic had the best accuracy in the RE band, while the RBA had the best accuracy in the NIR band. In study area 2, Blending had the lowest RMSE and MRPE of 0.035 and 16.5% in the RE band; however, in the NIR band, Color Balancing had the lowest RMSE and MRPE of 0.044 and

> REPLACE THIS LINE WITH YOUR MANUSCRIPT ID NUMBER (DOUBLE-CLICK HERE TO EDIT) <

15.5%.

Fig. 10 shows the results of 5-fold cross-validation. It can be found that the vignetting had a great influence on the calibration accuracy of RBA_NoVig, especially in the RE and NIR bands. Overall, RBA_Vig had the highest radiometric calibration accuracy, with mean RMSE and MRPE of 0.038, 15.1%, and 0.028, 15.5% in the two study areas, respectively; followed by RBA, with mean RMSE and MRPE of 0.039, 15.4%, and 0.031, 17.2%, respectively. Moreover, the calibration accuracy of the two in all bands was relatively close, which indicated that the feasibility and potential of vignetting correction using the RBA.

C. Uncertainty Analysis

There are 4 factors that influence the calibration accuracy of the RBA, and the uncertainties caused by these factors are listed in TABLE VI and TABLE VII. For each factor, 10 tests were conducted and the uncertainties were expressed as the average of the relative changes in RMSE before and after the changes in the corresponding factor.

- 1) Weight settings of error equations established by RTPs: the weights of the observations represent their reliability and therefore have an impact on the calibration accuracy of the RBA. When calculating the uncertainties, the weights of error equations were set to random numbers between [0, 1]. The uncertainties of different bands caused by the weight setting ranged from 1.046% to 5.233% for study area 1, and from 1.066% to 3.782% for study area 2.
- 2) Geometric mismatching: when extracting the DN values and pixel coordinates of RTPs or RCPs, the geometric mismatch can interfere with their information. The shifted window was used to obtain the uncertainty caused by geometric mismatching. When extracting the DN values of RTPs, the window was randomly shifted by 3 pixels on the row and column respectively. The range of the uncertainties of different bands caused by geometric mismatching in the two study areas was 0.598%~3.730% and 0.810%~2.770%, respectively.
- 3) Noise: the image quality can be influenced by the noise. In addition, the dark current is also a kind of noise in a sense. In this part, Gaussian noise with a mean of 0 and a standard deviation of 5% is added to the DN values of RTPs. The uncertainties caused by the noise ranged from 1.528% to 2.661% for study area 1 and 1.266% to 2.790% for study area 2. The uncertainties caused by noise were relatively small, which indicated that the RBA had a certain degree of noise immunity.
- 4) Equation solution: the iteration stopping condition is that the increments of unknowns are less than 10^{-5} or the iteration number is larger than 500. As a result, the uncertainty caused by the equation solution in the two study areas was near 0% in all bands.

The total uncertainties of different bands were between 2.307% and 6.664% in study area 1 and 2.427% and 4.732% in study area 2. Among them, the weights, geometric

mismatching, and noise had a relatively large impact on the radiometric correction accuracy, while the equation solution had little effect on the calibration results.

TABLE VI
INFLUENCE FACTORS AND THEIR UNCERTAINTY (%) OF STUDY AREA 1

Influence factor	B	G	R	RE	NIR
Weights	5.233	1.391	3.732	1.103	1.046
Geometric mismatching	3.730	1.452	1.492	0.598	0.776
Noise	1.766	1.528	2.661	2.035	1.904
Equation solution	0.000	0.000	0.000	0.000	0.000
Total uncertainty	6.664	2.525	4.820	2.390	2.307

TABLE VII
INFLUENCE FACTORS AND THEIR UNCERTAINTY (%) OF STUDY AREA 2

Influence factor	B	G	R	RE	NIR
Weights	3.426	3.782	1.066	1.786	2.620
Geometric mismatching	1.695	1.997	0.810	2.770	2.020
Noise	2.790	1.781	2.024	1.266	1.866
Equation solution	0.001	0.001	0.001	0.001	0.000
Total uncertainty	4.732	4.633	2.427	3.531	3.798

D. Potential of the Proposed Radiometric Block Adjustment

The RBA proposed in this paper can directly correct the vignetting at the same time as the radiometric calibration and does not require additional auxiliary measurements, thus reducing the complexity of the experiment and data processing. In addition, RBA requires only a small number of calibration blankets as input, making it a practical radiometric calibration method. At the same time, RBA allows the addition of reference targets of known reflectance in the study area, giving it some flexibility.

When there were obvious radiometric differences between images, the RBA could significantly improve the radiometric calibration accuracy, such as in the visible light bands; and when the radiometric differences between images were not obvious, the proposed method could also obtain reasonably radiometric calibration results, such as in the RE and NIR bands. Vegetation, as the main ground object in the two study areas of this paper, had low reflectance in visible light bands and high reflectance in the RE and NIR bands. Therefore, changes in factors such as illumination could easily make the images in visible light bands have obvious light-dark differences, while the light-dark differences in the RE and NIR bands were not obvious. Thus, the method proposed in this paper performed better in visible light bands. At the same time, the experimental results also showed that the RBA proposed in this paper was more suitable for the situation where there were obvious light-dark differences between images.

Blending and Color Balancing could obtain the mosaics with good visual quality when the radiometric differences between

> REPLACE THIS LINE WITH YOUR MANUSCRIPT ID NUMBER (DOUBLE-CLICK HERE TO EDIT) <

images were small (Fig. 3 (b) and (c)). However, when the radiometric differences became large, only good visual quality can be obtained locally, as shown in Fig. 5 (b) and (c). This is because Blending and Color Balancing mainly eliminate the radiometric differences between adjacent images. The RBA eliminates the radiometric differences between images from the whole, so it can obtain mosaics with good visual quality. In addition, RBA can effectively control the radiometric error propagation and accumulation and has great potential in the radiometric calibration of large-scale UAV images.

Satellites are affected by many factors when collecting images, so there will be different degrees of light-dark differences between images. Zhang et al. proposed a BA-based radiometric normalization method and validated its feasibility on Landsat-8 OLI images [54]. In addition, Han et al. proposed a cross-calibration method based on BA [50, 55]. In this paper, we proposed a BA-based radiometric calibration method suitable for multiple UAV images. However, due to the influences of various factors, such as atmospheric conditions, there are large differences between UAV images and satellite images. Therefore, the proposed method may not be directly applicable to satellite images. Further exploration is required if the method in this paper is to be applied to satellite data. However, it is feasible to eliminate the radiometric differences between satellite images based on the idea of BA.

VI. CONCLUSION

Based on the theory of BA, the radiometric block adjustment model between the DN value and the surface reflectance was built under the consideration of vignetting and light-dark differences between images and achieved the radiometric calibration of multiple UVA images using only a few calibration blankets. When obvious light-dark differences existed between images, such as visible light bands, the accuracy of radiometric calibration could be improved significantly by using the proposed method in this paper. The proposed method could also obtain reasonable results when the differences of brightness between images were small. The mean RMSE and MRPE were 0.053, 21.6%, and 0.037, 20.4% in the two study areas. After radiometric calibration, the homogeneity of the two datasets improved from 13.16%~21.82% to 5.47%~12.72%. And the total uncertainties ranged from 2.307% to 6.664% in the two study areas. Increasing the number of RCPs could effectively control the error propagation and accumulation and improve the calibration accuracy. We recommended adding a total of 4 RCPs of different types to the four corners of the study area, to improve the accuracy while keeping the workload at an appropriate level. At the same time, the results have shown that the proposed method has great potential in correcting image vignetting.

In the paper, we designed a weight setting method to reduce the influence of view geometry. However, it remains a challenge to accurately correct the BRDF in the UAV images while radiometric calibration. In addition, although UAVs taking images at low altitudes can reduce the influence of the atmosphere, significant atmospheric effects had been found

even at 50 m flight altitude [56]. Therefore, eliminating the BRDF and atmosphere effects in UAV images is very important to obtain accurate surface reflectance. And this will be the focus of our future research.

ACKNOWLEDGMENT

The authors would like to thank the Lab of Remote Sensing for Crop Phenotyping, School of Remote Sensing and Information Engineering, Wuhan University, China for providing the equipment. They would also like to thank the group directed by Shenghui Fang who assisted in the acquisition of data and provided suggestions for this research. They would also like to thank the anonymous reviewers for their efforts to improve the manuscript.

REFERENCES

- [1] W. H. Maes, and K. Steppe, "Perspectives for Remote Sensing with Unmanned Aerial Vehicles in Precision Agriculture," *Trends Plant Sci.*, vol. 24, no. 2, pp. 152-164, 2019, doi: 10.1016/j.tplants.2018.11.007.
- [2] J. Gago *et al.*, "UAVs challenge to assess water stress for sustainable agriculture," *Agric. Water Manage.*, vol. 153, pp. 9-19, 2015, doi: 10.1016/j.agwat.2015.01.020.
- [3] A. Mukherjee, S. Misra, and N. S. Raghuvanshi, "A survey of unmanned aerial sensing solutions in precision agriculture," *Journal of Network and Computer Applications*, vol. 148, 2019, doi: 10.1016/j.jnca.2019.102461.
- [4] L. P. Osco *et al.*, "A CNN approach to simultaneously count plants and detect plantation-rows from UAV imagery," *ISPRS J. Photogramm. Remote Sens.*, vol. 174, pp. 1-17, 2021, doi: 10.1016/j.isprsjprs.2021.01.024.
- [5] G. Yang *et al.*, "Unmanned Aerial Vehicle Remote Sensing for Field-Based Crop Phenotyping: Current Status and Perspectives," *Front. Plant Sci.*, vol. 8, pp. 1111, 2017, doi: 10.3389/fpls.2017.01111.
- [6] S. Mader *et al.*, "High-Throughput Phenotyping of Plant Height: Comparing Unmanned Aerial Vehicles and Ground LiDAR Estimates," *Front. Plant Sci.*, vol. 8, pp. 2002, 2017, doi: 10.3389/fpls.2017.02002.
- [7] S. Manfreda *et al.*, "On the Use of Unmanned Aerial Systems for Environmental Monitoring," *Remote Sens.*, vol. 10, no. 4, pp. 641, 2018, doi: 10.3390/rs10040641.
- [8] U. Niethammer, M. R. James, S. Rothmund, J. Travelletti, and M. Joswig, "UAV-based remote sensing of the Super-Sauze landslide: Evaluation and results," *Eng. Geol.*, vol. 128, pp. 2-11, 2012, doi: 10.1016/j.enggeo.2011.03.012.
- [9] S. Martin, J. Bange, and F. Beyrich, "Meteorological profiling of the lower troposphere using the research UAV "M(2)AV Carolo"," *Atmos. Meas. Tech.*, vol. 4, no. 4, pp. 705-716, 2011, doi: 10.5194/amt-4-705-2011.
- [10] A. T. Mozas-Calvache, J. L. Perez-Garcia, F. J. Cardenal-Escarcena, E. Mata-Castro, and J. Delgado-Garcia, "Method for photogrammetric surveying of archaeological sites with light aerial platforms," *J. Archaeol. Sci.*, vol. 39, no. 2, pp. 521-530, 2012, doi: 10.1016/j.jas.2011.10.007.
- [11] F. Chiabrando, F. Nex, D. Piatti, and F. Rinaudo, "UAV and RPV systems for photogrammetric surveys in archaeological areas: two tests in the Piedmont region (Italy)," *J. Archaeol. Sci.*, vol. 38, no. 3, pp. 697-710, 2011, doi: 10.1016/j.jas.2010.10.022.
- [12] Y. Guo, J. Senthilnath, W. Wu, X. Zhang, Z. Zeng, and H. Huang, "Radiometric Calibration for Multispectral Camera of Different Imaging Conditions Mounted on a UAV Platform," *Sustainability*, vol. 11, no. 4, 2019, doi: 10.3390/su11040978.
- [13] P. M. Teillet, "Image correction for radiometric effects in remote sensing," *Int. J. Remote Sens.*, vol. 7, no. 12, pp. 1637-1651, 1986, doi: 10.1080/01431168608948958.
- [14] M. Mafanya, P. Tsele, J. O. Botai, P. Manyama, G. J. Chirima, and T. Monate, "Radiometric calibration framework for ultra-high-resolution UAV-derived orthomosaics for large-scale mapping of invasive alien plants in semi-arid woodlands: *Harrisia pomanensis* as a case study," *Int. J. Remote Sens.*, vol. 39, no. 15-16, pp. 5119-5140, 2018, doi: 10.1080/01431161.2018.1490503.

> REPLACE THIS LINE WITH YOUR MANUSCRIPT ID NUMBER (DOUBLE-CLICK HERE TO EDIT) <

- [15] G. M. Smith, and E. J. Milton, "The use of the empirical line method to calibrate remotely sensed data to reflectance," *Int. J. Remote Sens.*, vol. 20, no. 13, pp. 2653-2662, 1999, doi: 10.1080/014311699211994.
- [16] B. Duan, S. Fang, Y. Gong, Y. Peng, X. Wu, and R. Zhu, "Remote estimation of grain yield based on UAV data in different rice cultivars under contrasting climatic zone," *Field Crops Res.*, vol. 267, pp. 108148, 2021, doi: 10.1016/j.fcr.2021.108148.
- [17] J. A. J. Berni, P. J. Zarco-Tejada, L. Suarez, and E. Fereres, "Thermal and Narrowband Multispectral Remote Sensing for Vegetation Monitoring From an Unmanned Aerial Vehicle," *IEEE Trans. Geosci. Remote Sens.*, vol. 47, no. 3, pp. 722-738, 2009, doi: 10.1109/tgrs.2008.2010457.
- [18] C. Y. Wang, and S. W. Myint, "A Simplified Empirical Line Method of Radiometric Calibration for Small Unmanned Aircraft Systems-Based Remote Sensing," *IEEE J. Sel. Top. Appl. Earth Obs. Remote Sens.*, vol. 8, no. 5, pp. 1876-1885, 2015, doi: 10.1109/jstars.2015.2422716.
- [19] L. Deng, X. Hao, Z. Mao, Y. Yan, J. Sun, and A. Zhang, "A Subband Radiometric Calibration Method for UAV-Based Multispectral Remote Sensing," *IEEE J. Sel. Top. Appl. Earth Obs. Remote Sens.*, vol. 11, no. 8, pp. 2869-2880, 2018, doi: 10.1109/jstars.2018.2842466.
- [20] Y. Jeong, J. Yu, L. Wang, H. Shin, S. M. Koh, and G. Park, "Cost-effective reflectance calibration method for small UAV images," *Int. J. Remote Sens.*, vol. 39, no. 21, pp. 7225-7250, 2018, doi: 10.1080/01431161.2018.1516307.
- [21] K. Xu, Y. Gong, S. Fang, K. Wang, Z. Lin, and F. Wang, "Radiometric Calibration of UAV Remote Sensing Image with Spectral Angle Constraint," *Remote Sens.*, vol. 11, no. 11, pp. 1291, 2019, doi: 10.3390/rs11111291.
- [22] J. Rodriguez, I. Lizarazo, F. Prieto, and V. Angulo-Morales, "Assessment of potato late blight from UAV-based multispectral imagery," *Comput. Electron. Agric.*, vol. 184, pp. 106061, 2021, doi: 10.1016/j.compag.2021.106061.
- [23] W. Pines, R. LaClair, C. Willey, B. Mamaghani, and C. Salvaggio, "Automated Calibration Pipeline For Agricultural sUAS Based Remote Sensing," *Proceedings of SPIE*, 2021.
- [24] J. I. Shin *et al.*, "Relative Radiometric Calibration Using Tie Points and Optimal Path Selection for UAV Images," *Remote Sens.*, vol. 12, no. 11, pp. 1726, 2020, doi: 10.3390/rs12111726.
- [25] F. Iqbal, A. Lucieer, and K. Barry, "Simplified radiometric calibration for UAS-mounted multispectral sensor," *Eur. J. Remote Sens.*, vol. 51, no. 1, pp. 301-313, 2018, doi: 10.1080/22797254.2018.1432293.
- [26] Y. H. Tu, S. Phinn, K. Johansen, and A. Robson, "Assessing Radiometric Correction Approaches for Multi-Spectral UAS Imagery for Horticultural Applications," *Remote Sens.*, vol. 10, no. 11, 2018, doi: 10.3390/rs10111684.
- [27] E. Honkavaara *et al.*, "Processing and Assessment of Spectrometric, Stereoscopic Imagery Collected Using a Lightweight UAV Spectral Camera for Precision Agriculture," *Remote Sens.*, vol. 5, no. 10, pp. 5006-5039, 2013, doi: 10.3390/rs5105006.
- [28] J. Svendsgaard, S. M. Jensen, S. Christensen, and J. Rasmussen, "The importance of spectral correction of UAV-based phenotyping with RGB cameras," *Field Crops Res.*, vol. 269, pp. 108177, 2021, doi: 10.1016/j.fcr.2021.108177.
- [29] Y. Taddia, P. Russo, S. Lovo, and A. Pellegrinelli, "Multispectral UAV monitoring of submerged seaweed in shallow water," *Applied Geomatics*, vol. 12, no. SUPPL 1, pp. 19-34, 2020, doi: 10.1007/s12518-019-00270-x.
- [30] J. Edwards, J. Anderson, W. Shuart, and J. Woolard, "An Evaluation of Reflectance Calibration Methods for UAV Spectral Imagery," *Photogramm. Eng. Remote Sens.*, vol. 85, no. 3, pp. 221-230, 2019, doi: 10.14358/pers.85.3.221.
- [31] B. Lu, and Y. H. He, "Species classification using Unmanned Aerial Vehicle (UAV)-acquired high spatial resolution imagery in a heterogeneous grassland," *ISPRS J. Photogramm. Remote Sens.*, vol. 128, pp. 73-85, 2017, doi: 10.1016/j.isprsjprs.2017.03.011.
- [32] R. A. dos Santos *et al.*, "Surface reflectance calculation and predictive models of biophysical parameters of maize crop from RG-NIR sensor on board a UAV," *Precis. Agric.*, vol. 22, no. 5, pp. 1535-1558, 2021, doi: 10.1007/s11119-021-09795-x.
- [33] Y.-H. Tu, S. Phinn, K. Johansen, A. Robson, and D. Wu, "Optimising drone flight planning for measuring horticultural tree crop structure," *ISPRS J. Photogramm. Remote Sens.*, vol. 160, pp. 83-96, 2020, doi: 10.1016/j.isprsjprs.2019.12.006.
- [34] N. Delavarpour, C. Koparan, J. Nowatzki, S. Bajwa, and X. Sun, "A Technical Study on UAV Characteristics for Precision Agriculture Applications and Associated Practical Challenges," *Remote Sens.*, vol. 13, no. 6, pp. 1204, 2021, doi: 10.3390/rs13061204.
- [35] Y. Zheng, S. Lin, S. B. Kang, R. Xiao, J. C. Gee, and C. Kambhamettu, "Single-Image Vignetting Correction from Gradient Distribution Symmetries," *IEEE Trans. Pattern Anal. Mach. Intell.*, vol. 35, no. 6, pp. 1480-1494, 2013, doi: 10.1109/tpami.2012.210.
- [36] D. Olsen, C. Y. Dou, X. D. Zhang, L. B. Hu, H. Kim, and E. Hildum, "Radiometric Calibration for AgCam," *Remote Sens.*, vol. 2, no. 2, pp. 464-477, 2010, doi: 10.3390/rs2020464.
- [37] E. F. Berra, R. Gaulton, and S. Barr, "Commercial Off-the-Shelf Digital Cameras on Unmanned Aerial Vehicles for Multitemporal Monitoring of Vegetation Reflectance and NDVI," *IEEE Trans. Geosci. Remote Sens.*, vol. 55, no. 9, pp. 4878-4886, 2017, doi: 10.1109/tgrs.2017.2655365.
- [38] H. T. Cao, X. F. Gu, X. Q. Wei, T. Yu, and H. F. Zhang, "Lookup Table Approach for Radiometric Calibration of Miniaturized Multispectral Camera Mounted on an Unmanned Aerial Vehicle," *Remote Sens.*, vol. 12, no. 24, pp. 4012, 2020, doi: 10.3390/rs12244012.
- [39] J. Jiang *et al.*, "Analysis and Evaluation of the Image Preprocessing Process of a Six-Band Multispectral Camera Mounted on an Unmanned Aerial Vehicle for Winter Wheat Monitoring," *Sensors*, vol. 19, no. 3, pp. 747, 2019, doi: 10.3390/s19030747.
- [40] J. Kelcey, and A. Lucieer, "SENSOR CORRECTION AND RADIOMETRIC CALIBRATION OF A 6-BAND MULTISPECTRAL IMAGING SENSOR FOR UAV REMOTE SENSING," *Xxii Isprs Congress, Technical Commission I*, International Archives of the Photogrammetry, Remote Sensing and Spatial Information Sciences M. Shortis and N. ElSheimy, eds., pp. 393-398, 2012.
- [41] H. Aasen, E. Honkavaara, A. Lucieer, and P. J. Zarco-Tejada, "Quantitative Remote Sensing at Ultra-High Resolution with UAV Spectroscopy: A Review of Sensor Technology, Measurement Procedures, and Data Correction Workflows," *Remote Sens.*, vol. 10, no. 7, pp. 1091, 2018, doi: 10.3390/rs10071091.
- [42] S. Wang *et al.*, "Unmanned Aerial System multispectral mapping for low and variable solar irradiance conditions: Potential of tensor decomposition," *ISPRS J. Photogramm. Remote Sens.*, vol. 155, pp. 58-71, 2019, doi: 10.1016/j.isprsjprs.2019.06.017.
- [43] B. Yang, M. Wang, W. Xu, D. R. Li, J. Y. Gong, and Y. D. Pi, "Large-scale block adjustment without use of ground control points based on the compensation of geometric calibration for ZY-3 images," *ISPRS J. Photogramm. Remote Sens.*, vol. 134, pp. 1-14, 2017, doi: 10.1016/j.isprsjprs.2017.10.013.
- [44] Y. D. Pi, B. Yang, X. Li, M. Wang, and Y. F. Cheng, "Large-Scale Planar Block Adjustment of GaoFen1 WFV Images Covering Most of Mainland China," *IEEE Trans. Geosci. Remote Sens.*, vol. 57, no. 3, pp. 1368-1379, 2019, doi: 10.1109/tgrs.2018.2866286.
- [45] G. Zhang *et al.*, "Block Adjustment for Satellite Imagery Based on the Strip Constraint," *IEEE Trans. Geosci. Remote Sens.*, vol. 53, no. 2, pp. 933-941, 2015, doi: 10.1109/tgrs.2014.2330738.
- [46] H. Cao, P. J. Tao, H. H. Li, and J. Shi, "Bundle adjustment of satellite images based on an equivalent geometric sensor model with digital elevation model," *ISPRS J. Photogramm. Remote Sens.*, vol. 156, pp. 169-183, 2019, doi: 10.1016/j.isprsjprs.2019.08.011.
- [47] L. Chandelier, and G. Martinoty, "A Radiometric Aerial Triangulation for the Equalization of Digital Aerial Images and Orthoimages," *Photogramm. Eng. Remote Sens.*, vol. 75, no. 2, pp. 193-200, 2009, doi: 10.14358/pers.75.2.193.
- [48] D. H. Lopez, B. F. Garcia, J. G. Piqueras, and G. V. Alcazar, "An approach to the radiometric aerotriangulation of photogrammetric images," *ISPRS J. Photogramm. Remote Sens.*, vol. 66, no. 6, pp. 883-893, 2011, doi: 10.1016/j.isprsjprs.2011.09.011.
- [49] A. Pros, I. Colomina, J. A. Navarro, R. Antequera, and P. Andrial, "RADIOMETRIC BLOCK ADJUSTMENT AND DIGITAL RADIOMETRIC MODEL GENERATION," *Isprs Hannover Workshop 2013*, International Archives of the Photogrammetry Remote Sensing and Spatial Information Sciences W-1, C. Heipke, K. Jacobsen, F. Rottensteiner and U. Sörgel, eds., pp. 293-298, 2013.
- [50] J. Han, Z. Tao, Y. Xie, Q. Y. Liu, and Y. J. Huang, "Radiometric Cross-Calibration of GF-4/PMS Based on Radiometric Block Adjustment," *IEEE Trans. Geosci. Remote Sens.*, vol. 59, no. 6, pp. 4522-4534, 2021, doi: 10.1109/tgrs.2020.3009740.
- [51] E. Honkavaara, and E. Khoramshahi, "Radiometric Correction of Close-Range Spectral Image Blocks Captured Using an Unmanned Aerial Vehicle with a Radiometric Block Adjustment," *Remote Sens.*, vol. 10, no. 2, pp. 256, 2018, doi: 10.3390/rs10020256.

> REPLACE THIS LINE WITH YOUR MANUSCRIPT ID NUMBER (DOUBLE-CLICK HERE TO EDIT) <

- [52] J. Pan, M. Wang, D. R. Li, and J. L. Li, "A Network-Based Radiometric Equalization Approach for Digital Aerial Orthoimages," *IEEE Geosci. Remote Sens. Lett.*, vol. 7, no. 2, pp. 401-405, 2010, doi: 10.1109/LGRS.2009.2037442.
- [53] L. Deng, Z. Mao, X. Li, Z. Hu, F. Duan, and Y. Yan, "UAV-based multispectral remote sensing for precision agriculture: A comparison between different cameras," *ISPRS J. Photogramm. Remote Sens.*, vol. 146, pp. 124-136, 2018, doi: 10.1016/j.isprsjprs.2018.09.008.
- [54] X. Zhang, R. Feng, X. Li, H. Shen, and Z. Yuan, "Block Adjustment-Based Radiometric Normalization by Considering Global and Local Differences," *IEEE Geosci. Remote Sens. Lett.*, vol. 19, pp. 1-5, 2020, doi: 10.1109/LGRS.2020.3031398.
- [55] Y. Xie, J. Han, X. F. Gu, and Q. Y. Liu, "On-Orbit Radiometric Calibration for a Space-Borne Multi-Camera Mosaic Imaging Sensor," *Remote Sens.*, vol. 9, no. 12, 2017, doi: 10.3390/rs9121248.
- [56] J. Suomalainen *et al.*, "Direct reflectance transformation methodology for drone-based hyperspectral imaging," *Remote Sens. Environ.*, vol. 266, pp. 112691, 2021, doi: <https://doi.org/10.1016/j.rse.2021.112691>.



Wanshan Peng received the B.S. degree from the University of Electronic Science and Technology of China (UESTC), Chengdu, China and the master degree from the Wuhan University (WHU), Wuhan, China.

His main research interest is the radiometric calibration of multiple UAV images.



Yan Gong received the B.S., and Ph.D. degrees in photogrammetry and remote sensing from WHU, Wuhan, China, in 2002 and 2007, respectively.

He is currently a Professor of photogrammetry and remote sensing with the School of Remote Sensing and Information Engineering, WHU. His research interests include hyperspectral remote sensing on agriculture, the phenotype analysis of hybrid rice, radiometric calibration of satellite and UAV images and the atmosphere correction of remote sensing images.



Shenghui Fang received the B.S. and M.S., degrees from Wuhan Technical University of Surveying and Mapping (WTUSM), Wuhan, China, in 1986, and 1997, respectively and the Ph.D. degrees from WHU in 2007.

He is currently a Professor of photogrammetry and remote sensing with the School of Remote Sensing and Information Engineering, WHU. His research interests include hyperspectral remote sensing on agriculture, the phenotype analysis of hybrid rice and the quantitative remote sensing.



Yongjun Zhang received the B.S., M.S., and Ph.D. degrees in photogrammetry and remote sensing from WHU, Wuhan, China, in 1997, 2000, and 2002, respectively.

He is currently a Professor of photogrammetry and remote sensing with the School of Remote Sensing and Information Engineering, WHU. His research interests include aerospace and low-altitude photogrammetry, image matching, combined block adjustment with multisource data sets, integration of LiDAR point clouds and images, and three-dimensional city reconstruction.



Jadunandan Dash received the M.Tech. degree from IIT Kanpur, Kanpur, India, in 2002, and the Ph.D. degree from the University of Southampton, Southampton, U.K., in 2005.

He is currently a Professor of Remote Sensing with the University of Southampton. He is also with the European Space Agency to develop vegetation biophysical variables from satellite data including the recently launched Sentinel 2 and 3 optical sensors. His research interests include the time series analysis of satellite data to derive vegetation phenological variable and developing model for estimation of gross primary productivity and estimation of crop yield for major grain crops.



Jie Ren received the B.S. from the WHU and is now working on his M.S. at WHU.

His main research interests include the radiometric calibration of satellite and UAV images and the atmosphere correction.



Jiakai Mo received the B.S. degree from the Tongji University, Shanghai, China and the M.S. from WHU.

His main research interests include the crop phenotype and phenology and the precision agriculture.